Journal of Nuclear Materials 570 (2022) 153944

Contents lists available at ScienceDirect

Journal of Nuclear Materials

journal homepage: www.elsevier.com/locate/jnucmat

Emulation of neutron-irradiated microstructure of austenitic 21Cr32Ni model alloy using dual-ion irradiation

Muhammet Ayanoglu*, Arthur T. Motta

Ken and Mary Alice Lindquist Department of Nuclear Engineering, The Pennsylvania State University Park, PA, USA

ARTICLE INFO

Article history:
Received 8 April 2022
Revised 27 June 2022
Accepted 23 July 2022
Available online 25 July 2022

Keywords:
Dual-ion irradiation
21Cr32Ni model alloy
Austenitic stainless steel
Fast neutron irradiation
Cavity
Faulted dislocation loop
BOR-60
precipitation
and elemental segregation

ABSTRACT

In this study, the capability of heavy-ion irradiation to emulate neutron irradiation was demonstrated on an austenitic 21Cr32Ni type ternary model alloy. The model alloy used in this study is chemically analogous but compositionally simpler than of alloy 800H, which is a candidate austenitic Ni alloy which has been proposed for use in Generation IV reactors.

The microstructure of the 21Cr32Ni model alloy irradiated in the BOR-60 fast reactor to 17.1 dpa and 35 dpa at ~380 °C was characterized using transmission electron microscopy (TEM). The 17.1 dpa BOR-60 irradiated microstructure was then compared with the microstructure of the same material developed under dual-ion (DI) irradiation using various He/dpa ratios between 0.1 and 16.6 appm He/dpa in the temperature range of 430 °C-500 °C. The results showed that both neutron and DI irradiation of 21Cr32Ni model alloy produced dislocations in the form of a dislocation network as well as {111}-type faulted dislocation loops, cavities, and radiation-induced Ni enrichment at radiation-induced sinks. When the dose and the He/dpa ratio were kept similar to those in neutron irradiation, DI irradiation of the 21Cr32Ni model alloy at 460 °C resulted in over-nucleation of small cavities and in a high density of faulted dislocation loops compared to those observed in the fast-neutron irradiated alloy of the same heat irradiated at ~380 °C. The optimal condition for reproducing the neutron-irradiated microstructure was DI irradiation at 460 °C and 0.1 appm He/dpa. In that case, the faulted loop and cavity size distributions in the BOR-60 irradiated 21Cr32Ni model alloy samples closely matched with those measured in the DI irradiated 21Cr32Ni model alloy sample. The fact that the He/dpa is an order of magnitude smaller than the helium generation rate for fast neutron irradiation, stops over nucleation and allows for the development of a similar microstructure as for neutron irradiation.

1. Introduction

Heavy-ion irradiation has been widely used to investigate radiation effects in materials because it provides much higher damage rates than neutron irradiation (10^{-3}–10^{-4} dpa/s vs. 10^{-6}–10^{-7} dpa/s), allowing researchers to perform irradiation experiments in hours and days, instead of months or years, with little or no residual activity. On the other hand, microstructures developed at high damage rates can be quite different than those developed at low damage rates due to the following differences between neutron and ion irradiation:

1. *Dose rate*: Neutron and ion irradiation can have a difference in dose rate by a factor of 10^3–10^4 (~10^{-7} to 10^{-8} dpa/s for neutrons and ~10^{-3} to 10^{-4} dpa/s for ion irradiation depending on the reactor and the type of ion irradiation.). High damage rates mean high defect production rates but also high recombination rates, which requires the application of temperature shift.
2. *Recoil spectrum*: The energy of the recoils generated by neutrons and protons can be quite different leading to variations in the consequent defect evolution. Heavy ions with high energies are used to produce a similar recoil spectrum to that produced by high-energy neutrons.
3. *Helium generation*: Helium being generated through (n, α) reactions (and other transmutation reactions) in nuclear reactors cannot be generated during ion irradiation which often requires dual-ion irradiation experiments where helium ions are co-injected.
4. *Interaction of radiation damage with the microstructure*: Clearly neutron and ion irradiations can produce different microstructural and microchemical variations, depending on the various interactions between the irradiation-produced defects and the evolving microstructure.

The fact that the irradiated microstructure is a result of the balance between damage and thermal annealing, and as a result, it is

* Corresponding author.
E-mail address: ayanoglum@ornl.gov (M. Ayanoglu).

https://doi.org/10.1016/j.jnucmat.2022.153944
0022-3115/

necessary to increase the latter to match an increase in the former [1,2]. For a given change in dose rate, Mansur posited that the net defect flux to defect sinks (such as dislocations and cavities) can be maintained by a change in irradiation temperature according to:

$$\text{Dislocations and cavities} \rightarrow T_2 - T_1 = \frac{\frac{k_B T_1^2}{E_v^m + nE_v^f} \ln\left(\frac{G_2}{G_1}\right)}{\frac{k_B T_1}{E_v^m + nE_v^f} \ln\left(\frac{G_2}{G_1}\right)} \quad (1)$$

Here, subscripts "1" and "2" denote neutron and ion irradiation, respectively. T's are the irradiation temperatures in ^oK, the G's are the damage rates (dpa/s), k_B is Boltzmann's constant (8.62×10^{-5} eV/K), and E_v^m and E_v^f are the vacancy migration and formation energies (this derivation assumes that the vacancies are slower migrating than interstitials). The value of n in Eq. (1) is determined by the dominant process of point defect loss as such; for sink-dominated regime $n=1$; whereas for recombination-dominated regime, $n=2$. A different equation was also proposed as valid for radiation-induced segregation (RIS) in [1,2] but we made a conscious decision to try to reproduce the loop and cavity microstructure instead of RIS.

It is important to note that different microstructure and microchemical evolution mechanisms take different times because they are mediated by the motion of various chemical species with different migration energies. Therefore, a global temperature shift that matches every microstructural feature is not achievable. Thus, the temperature shift given in Eq. (1) only addresses the first one of the differences above, albeit the largest one. Although it addresses it imperfectly, there has been no more rigorous treatment method of the different dose rates. For example, the rigorous rate theory calculations have numerous approximations. Three important assumptions or simplifications were made when deriving the Eq. (1): (a) microstructures are assumed to be at steady-state, (b) sink strengths are assumed to be constant, and sinks are assumed to be uniformly distributed in the microstructure with no spatial variation, (c) no helium present in the microstructure i.e. the role of He in stabilizing cavities is ignored. Because of these simplifications, the validity of this equation was investigated by many authors. N. H. Packan [3] compared the experimental peak swelling temperature vs. damage rate for different heats of nickel samples and reported that the experimental peak swelling temperature increases linearly with respect to the logarithm of the damage rate, as predicted by Eq. (1). There are only a few studies performed using heavy-ion irradiation that are specifically designed to simulate neutron irradiation using the same alloy heat. A recent study compared dislocation and cavity microstructures produced in a ferritic-martensitic T91 alloy irradiated in the BOR-60 fast reactor up to 35 dpa at 376 °C to those produced in a dual-ion irradiated alloy of the same heat within the temperature range of 406–560 °C [4,5–6]. The authors reported that the neutron-induced dislocation and cavity microstructures in T91 are similar to those in dual-ion irradiated T91 samples when using a temperature shift of ~60–70 °C. On the other hand, the helium co-injection rate used in the dual-ion irradiation experiments was ~4 appm He/dpa - considerably greater than the helium generation rate estimated in the BOR-60 fast reactor which was only 0.22 appm He/dpa. The authors attributed the requirement for higher helium injection rate to the differences in helium partitioning between neutron and ion irradiated T91 microstructures. Using a helium partitioning model, they showed that the helium atoms are initially trapped at different trapping sites (dislocation lines, dislocation loops, and He-V clusters and cavities) in proportion to their sink strengths. Over time, the trapped helium atoms are de-trapped and they flow from weaker traps (such as dislocation lines, dislocation loops, He-V clusters) to the stronger traps (cavities) based on the helium binding energy. In both ion and neutron irradiation, non-cavity sinks other than cavities are rapidly formed and start trapping helium atoms. At low damage rates, non-cavity sinks are saturated by helium at very doses (~0.5 dpa) since longer time between damage events allows helium atoms more time to be trapped/de-trapped from sinks and effectively partitioned to the strongest traps during irradiation. At high damage rates, however, non-cavity sinks cannot be saturated by helium until high doses (<~9 dpa) due to their high production rate. In this case, helium does not have time to be de-trapped to flow towards cavities to promote their growth since the time between damage events (and the total irradiation time) of ion experiments is very short. So, an additional helium injection has been suggested by the authors when using dual-ion irradiation at high damage rates to compensate for the loss of helium to other sinks.

While the recent heavy-ion irradiation studies provide valuable data for ferritic/martensitic (F/M) stainless steels, it is still necessary to extend our understanding of the capability of ion irradiation to simulate neutron irradiation of austenitic stainless steels in the presence of helium as the helium migration behavior in the bcc crystal structure can be substantially different than in the fcc crystal structure [7–9].

In this paper, the microstructure of austenitic 21Cr32Ni model alloy fast neutron irradiated to 17.1 and 35 dpa at ~380 °C was investigated using Transmission Electron Microscopy (TEM). The 17.1 dpa neutron irradiated microstructure was then compared with a series of dual-ion irradiated 21Cr32Ni model alloy microstructure to 16.6 dpa using different temperature shifts and He/dpa ratios to form a basis for relatively higher dose irradiation experiments in the future. Unlike ferritic/martensitic stainless steels, it is shown that the emulation of neutron-irradiated microstructure of the fcc austenitic alloys using heavy-ions requires a *reduction* of He/dpa ratio. Further discussion is presented in detail in the following sections.

2. Experimental

2.1. Material

The austenitic Fe-Cr-Ni ternary model alloy used in this study was provided by GE Global Research as heat #RAM-2192 with a nominal alloy composition of ~21 wt.% of Cr and ~32 wt.% of Ni, balance Fe. The 21Cr32Ni model alloy was prepared from an original bulk material with an initial size of 7.62 cm diameter and 1.84 cm thickness. A series of cold rolling processes were applied at room temperature followed by a heat treatment at ~1200 °C for ~2 h. A final cold rolling was performed to reach an overall thickness reduction of ~65% of the original thickness. Finally, solution annealing was conducted at ~950–1000 °C for 30 mins.

The elemental composition of the 21Cr32Ni model alloy provided by the manufacturer is given in Table 1. An additional atom probe tomography (APT) measurement carried out with the 21Cr32Ni model alloy prior to irradiation is also given in this table along with the reference alloy 800H composition [10] for comparison. Table 1 shows that the elemental composition of 21Cr32Ni model alloy provided by the manufacturer agrees well with the APT measurement. The composition of the major elements in the model alloy is similar to those measured on the reference alloy 800H, whereas the total minor alloying element content is below ~0.2 wt.% as opposed to alloy 800H where it is ~2 wt.% on average.

2.2. Sample preparation and description of the BOR-60 irradiation experiments

For neutron irradiation experiments in the BOR-60 fast reactor, thin slices (~0.5 mm) of 21Cr32Ni samples were cut from the heat-treated bulk material using a wire electrical discharge machine

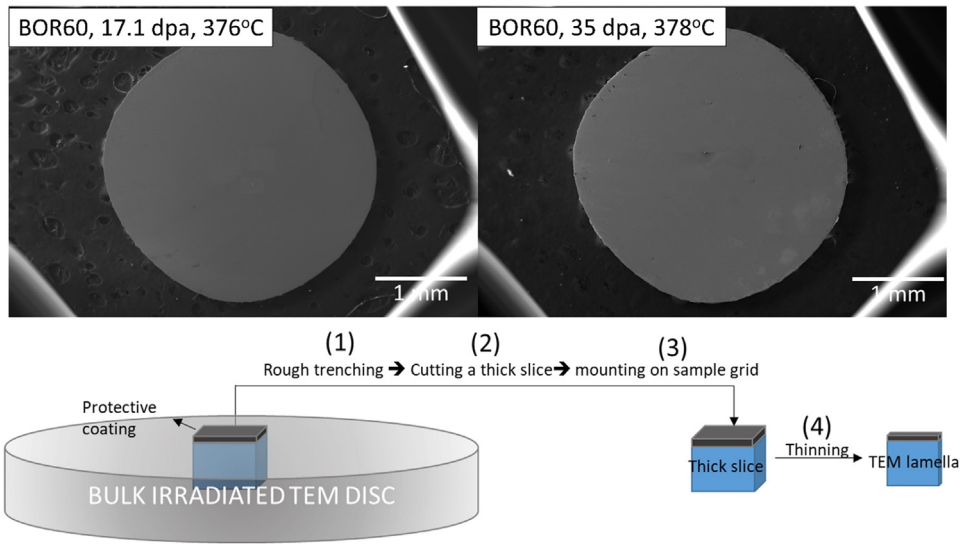

Fig. 1. (Top) Scanning electron microscope (SEM) images showing the surface of 3 mm diameter 21Cr32Ni TEM disks after BOR-60 irradiation to 17.1 dpa and 35 dpa, (bottom) Schematic illustration of TEM sample preparation from the neutron irradiated TEM disks using focused-ion beam technique.

Table 1
Elemental composition analysis of as-received 21Cr32Ni model alloy in weight percent in comparison with the commercial alloy 800H [9].

Element	21Cr32Ni model alloy (wt%)		800H (wt%)	
	As-received	APT	Min.	Max.
Fe	Bal.	Bal.	Bal.	Bal.
Ni	31.16	32.6	30.0	35.0
Cr	20.73	19.9	19.0	23.0
Mn	0.94	0.89	–	1.5
Al	–	–	0.15	0.60
Ti	–	–	0.15	0.60
Cu	0.01	–	–	0.75
Si	0.10	–	–	1.0
Mo	0.02	–	–	–
C	~0.01	0.03	0.05	0.1
P	~0.01	–	–	–
N	–	0.003	–	–
Ni	31.16	32.6	30.0	35.0
Total minor alloying element	**0.15**	**~0.033**	**0.35**	**4.55**

(EDM) and further thinned down from both sides to a thickness of 0.25 mm following by diamond lapping applied for a ~0.25 µm finish. Then, 3-mm diameter TEM disks were punched out from the thinned slices and inserted into the irradiation capsules. These sample capsules were put into the irradiation rigs which were then placed in the BOR-60 fast reactor at a core position to achieve the doses of 17.1 dpa and 35 dpa[1] at the irradiation temperatures of ~376 °C and ~378 °C.[2]

After BOR-60 irradiation, the sample capsules were shipped to the Irradiated Materials Examination Laboratory (IMET) at Los Alamos National Laboratory (LANL) and opened using a slow-speed cut in the hot cells. Post-irradiation characterization of the neutron-irradiated 21Cr32Ni samples was performed at the Low Activation Materials Design and Laboratory (LAMDA) facility at Oak Ridge National Laboratory (ORNL), using an FEI Talos F200x Scanning/Transmission Electron Microscope (S/TEM). The activities of the samples (in the form of 3 mm disks prior to sample preparation for TEM analysis) were measured by ORNL staff to be ~30 mrem/hr at the point of contact and ~10 mrem/hr at 30 cm, so that direct handling in ORNL LAMDA could be accomplished. TEM specimens were prepared from the irradiated TEM disks (see Fig. 1) using a Focused Ion Beam (FIB) on a Thermo-Scientific Quanta Dual Beam (shielded) Scanning Electron Microscope (SEM) and FEG Versa SEM. For this purpose, a carbon layer was initially applied on the sample using electron beam (e-beam) for ~7 min using 2 kV e-beam voltage and 51 nA e-beam current. Then, a second platinum deposition layer (~3 µm thick) was applied using 30 kV ion beam (I-beam) voltage and ~0.23 nA current. The rough trenching was performed using a 21 nA I-beam current, following by two rough thinning steps at 9.3 nA and 2.5 nA, respectively. After mounting the slice on a sample grid, thinning was performed at 30 kV I-beam voltage with 0.79 nA and 0.23 nA. Once the sample turned brighter, the I-beam voltage and the I-beam current were decreased to 5 kV and 0.12 nA with the final thinning at 2 kV until the sample thickness was reduced to ~100 nm or less, for electron transparency.

2.3. Sample preparation and description of the bulk-ion irradiation experiments

For bulk-ion irradiation experiments, sample bars were cut from the initial heat-treated bulk material using a wire electrical discharge machine (EDM). Then, their surfaces were mechanically polished to a 0.02 µm surface finish, followed by electrochemical polishing at approximately −40 °C at 30 V for about 15 s using 10% perchloric acid in a methanol solution prior to irradiation as described in [5]. Each bar was then marked with an individual ID to describe its irradiation conditions as shown in Fig. 2.

The polished sample bars were then irradiated at Michigan Ion Beam Laboratory (MIBL) using a dual-ion beam. The dual-ion beam irradiation experiments were performed using Fe^{2+} self-ions and simultaneously injected He^{2+} ions (2–2.15 MeV) in defocused mode to achieve a uniform damage profile in the middle of the sample bars. The helium was co-injected at an angle of 60° relative to the sample normal with He/dpa ratios of 0.1, 1 and ~16.6 appm He/dpa while heavy-ions were injected perpendicular to the sample to maximize their penetration depth. The desired helium implantation profile was achieved using a rotatable thin Al foil

[1] The dose calculations were performed by the Research Institute of Atomic Reactors (RIAR) in Russia using a displacement energy value of 40 eV for Fe.

[2] The small difference in irradiation temperatures between these two irradiations was possibly due to the difference in their axial capsule positions in the irradiation rigs. The estimated uncertainty of the irradiation temperatures was reported to be ~7-25°C.

Table 2
Summary of bulk-ion irradiation experiments in comparison with neutron irradiation. (The doses given in the table were calculated at the target depth).

Dose [dpa]	T [°C]	Dose rate [dpa/s]	The depth at which targeted dose was achieved [nm]	Irradiating particle	Helium injection rate [appm He/dpa]
17.1	376	1×10^{-6}	–	Neutron (BOR-60)	1
16.6	460	7.8×10^{-4}	500–700	Fe^{2+}+ He^{2+}	0.1
16.6	460	5×10^{-4}	500–700	Fe^{2+}+ He^{2+}	1
16.6	500	5×10^{-4}	500–700	Fe^{2+}+ He^{2+}	1
16.6	430	5×10^{-4}	500–700	Fe^{2+}+ He^{2+}	16.6
16.6	446	3.46×10^{-4}	500–700	Fe^{2+}+ He^{2+}	16.6
16.6	460	5×10^{-4}	1100–1300*	Fe^{2+}+ He^{2+}	16.6

* This experiment was performed using 9 MeV Fe^{2+} instead of 5 MeV Fe^{2+}, so that the target depth was slightly shifted to deeper regions.

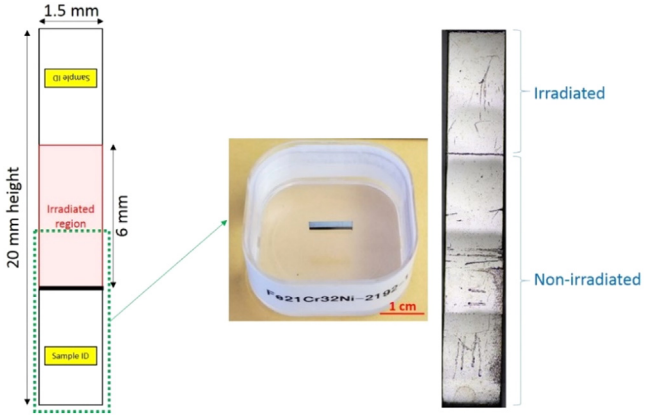

Fig. 2. Schematic illustration of 21Cr32Ni model alloy bar is given on the left. The photograph at the middle shows half of a sample bar (indicated with the arrow) in a TEM membrane box after bulk ion irradiation with the corresponding optical microscope image given on the right, showing the irradiated and non-irradiated section of the sample bar.

(~2.6 μm thick). The details of the helium implantation methodology were given in Reference [11]. Avoiding duplication, a brief description is offered as follows: When the helium ion beam hits the foil, it loses its energy through electronic and nuclear collisions and eventually scatters toward samples. The amount of energy loss of helium ion beam is proportional to the projected thickness of the foil as it rotates. As the rotation angle increases, helium energy decreases due to more energy loss in the foil, and the number of helium atoms decreases due to more scattering. By changing the rotation angle of the Al foil, the energy of the helium atoms at sample can be manipulated to achieve the desired helium implantation depth. To achieve a uniform helium implantation profile in the targeted depth, the time spent at each foil rotation angle is adjusted. Because less helium reaches to sample surface at high foil rotation angle, the time spent increases with increasing the rotation angle.

The dose, temperature, and helium injection rates used in the dual-ion irradiation experiments are summarized in Table 2. Although the total dose achieved in dual-ion irradiation experiments was similar to that in the BOR-60 neutron irradiation, the damage rates were ~500x greater than the BOR-60 damage rates as shown in Table 2. Therefore, a higher temperature was used during the heavy-ion irradiation experiments to compensate high damage rate effects. The required temperature shifts in this table were estimated using Eq. (1) to reproduce the irradiation-induced dislocation loops and cavities in the BOR-60 reactor using the parameters: T_1=380 °C, E_v^m=1.2 eV [12], E_v^f=1.8 eV [13] and $\frac{G_2}{G_1}$=500. In this scenario, the temperature shift was estimated to be ~50 °C (380 °C + 50 °C = 430 °C) for a recombination-dominated regime (n=2) and ~80 °C (380 °C + 80 °C = 460 °C) for a sink-dominated regime (n=1).

The penetration depth of Fe^{2+} heavy-ions and the corresponding damage profile were calculated using the Stopping and Range of Ions in Matter (SRIM) [14] in the "*quick calculation of damage*" mode as suggested by Stoller et al. [15] using the displacement energy of 40 eV for Fe, Cr and Ni. Fig. 3 shows the damage depth profiles of Fe^{2+} self-ions along with the He^{2+} implantation profile in the 21Cr32Ni model alloy. The figure also shows the depth at which the target dose was achieved and the implanted helium region which were both selected to minimize both surface and injected interstitial effects. The displacement damage produced by helium was small compared to damage by high energetic heavy ions, so it was excluded from the damage calculation.

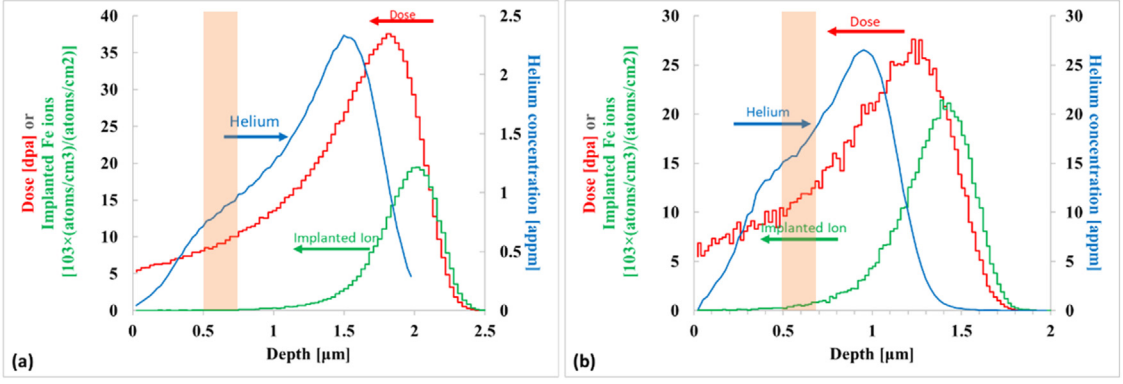

Fig. 3. Iron and helium depth profiles for dual-ion irradiations using defocused Fe^{2+} self-ions and energy degraded 2.00–2.15 MeV He^{2+} in 21Cr32Ni model alloy. The helium injection profile follows the damage curve to achieve constant He/dpa ratio (a) 9 MeV Fe^{2+} irradiation at 460 °C with 0.1 appm He/dpa injection rate and (b) 5 MeV Fe^{2+} irradiation at 460 °C with 1 appm He/dpa injection rate. The depth at which targeted dose was achieved is selected to be 500 nm-700 nm as highlighted in the figure.

After the bulk-ion irradiation, samples were characterized using either a FEI Tecnai G20 20 XTWIN TEM or a FEI Talos F200x S/TEM at the Penn State Material Characterization Laboratory (MCL). For this purpose, the TEM thin foils were prepared from the irradiated part of the sample (see the optical microscope image given in Fig. 2) using FIB. The FIB samples were prepared on either an FEI Helios NanoLab660 or an FEI Scios – both located at the MCL. The lift-out procedures used for the bulk-ion irradiated samples were the same as those used for neutron irradiated samples, as described in the previous section.

3. Experimental results and discussion

3.1. Dislocation microstructure in the BOR-60 irradiated 21Cr32Ni model alloy

Fig. 4 shows irradiation-induced dislocations observed in the 21Cr32Ni model alloy samples after neutron irradiation in the BOR-60 reactor to ~17.1 and 35 dpa. The neutron irradiation-induced dislocation microstructure consisted of high-density network dislocations and dislocation loops. Because the g=<200> diffraction vector near the [110] zone axis was used as the imaging condition, the vast majority of the dislocation loops in these micrographs appear to be edge-on, as highlighted with red circles in Fig. 4. These edge-on (or nearly edge-on) dislocation loops were identified to be {111}-type faulted dislocation loops. Although elliptical {111} loops from other variants were also likely present for the given imaging condition, they were difficult to detect due to the strong diffraction contrast of the high-density dislocation network. Although not experimentally verified in this study, previous irradiation studies performed on fcc austenitic stainless steels [16–19] showed that the radiation-induced {111}-type faulted dislocation loops are mainly interstitial-type, having Burger's vector of $\vec{b}=a/3[111]$.

To obtain better visibility and for easier quantification of the {111}-type faulted dislocation loops, a rel-rod dark-field (RDF) TEM imaging technique was used by tilting the samples to a two-beam condition using g=<311> diffraction vector, as shown in Fig. 5. In this figure, the irradiation-induced faulted dislocation loops are indicated with white arrows in the dark-field micrographs, while additional bright spots indicated in turquoise color correspond to the irradiation-induced precipitates, discussed in Section 3.3. Note that the faulted dislocation loops visible in these TEM images represent only ¼ of the total faulted dislocation loops in the microstructure since four different {111} loop variants are possible.

The number density and diameter of the faulted loops determined from Fig. 5 (a-b) using ImageJ software [20] are plotted in Fig. 5e with the tabulated data presented in Table 3 where the error bars were calculated as $\pm 2 \times$ standard error [21,22]. Fig. 5e clearly shows an increase in the faulted loop number density and a decrease in the average faulted loop diameter with increasing neutron irradiation dose. Previous bulk and in-situ ion irradiation experiments conducted on the 21Cr32Ni model alloy showed that the pre-existing large, faulted dislocation loops can become unfaulted as a result of an interaction with nearby dislocations during subsequent irradiation [21–27]. Once large faulted dislocation loops are unfaulted, then they become invisible to the rel-rod dark field technique. Meanwhile, small faulted dislocation loops were continuously generated, leading to an increase in loop number density with a decrease in average faulted loop diameter. The higher density of smaller faulted loop population at higher neutron irradiation dose is likely caused by similar unfaulting processes which took place on pre-existing large faulted loops formed at 17.1 dpa.

3.2. Cavity microstructure in BOR-60 irradiated 21Cr32Ni model alloy

Another significant change observed in the 21Cr32Ni model alloy microstructure after the BOR-60 irradiation was the formation of cavities, as shown in Fig. 6. The 17.1 dpa cavity microstructure showed a characteristic bimodal distribution where both small and large cavities co-existed in the microstructure (Fig. 6a). At 35 dpa, however, neutron-induced cavities were generally larger than those seen at 17.1 dpa (see

Table 3) and only a few small cavities were found in the 21Cr32Ni model alloy microstructure (Fig. 6b), causing the corresponding cavity size distribution to be relatively more unimodal as shown in Fig. 6c. The small cavities (<2 nm) were spherical in shape, while the large cavities (>2 nm) were faceted with facets aligned along the [111] plane; which is the close-packed plane in the fcc crystal. It is likely that the small cavities are small bubbles stabilized by helium gas pressure while the large cavities are those

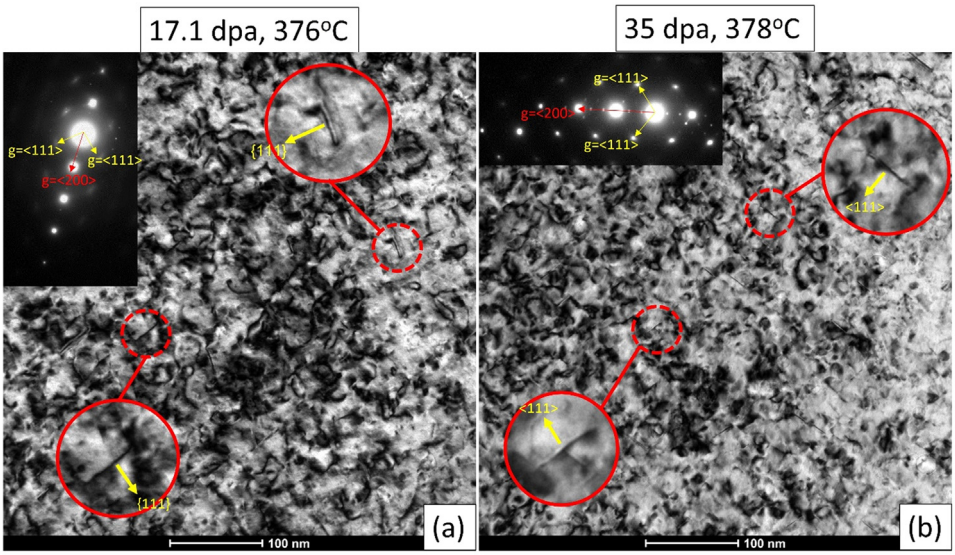

Fig. 4. Bright-field micrograph of the irradiation-induced dislocation microstructure of 21Cr32Ni model alloy after irradiation to (a) 17.1 at 376 °C and (b) 35 dpa at 378 °C in BOR-60 reactor, imaged using the g=<200> diffraction vector near the [110] zone axis. The diffraction patterns used for imaging are inset on the upper-left corner of each image. The micrographs show a high density of dislocations including both network dislocations and dislocation loops. The dislocation loops which are imaged edge-on are consistent with the {111} type habit plane. (Some of these {111} loops are highlighted with red circles for better visibility).

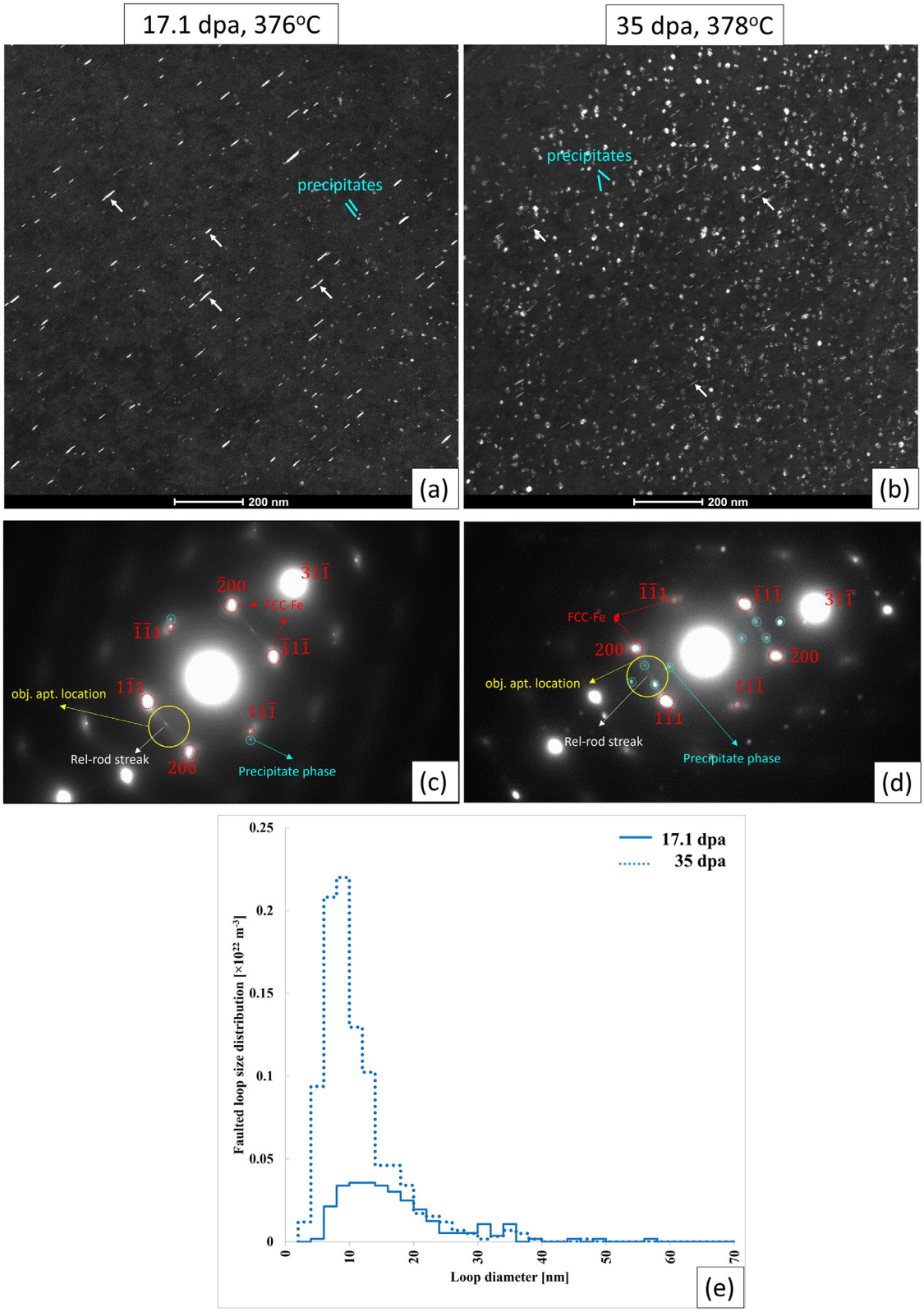

Fig. 5. (a-b) Rel-rod dark-field images showing the faulted loops (indicated with red) and precipitates (indicated in turquoise) in 21Cr32Ni model alloy microstructure after irradiation to 17 dpa at 376 °C and 35 dpa at 378 °C at BOR-60 reactor, (c-d) Corresponding indexed rel-rod diffraction patterns of the fcc structure. The circle represents the size and location of the objective aperture to produce rel-rod dark field images given in (a-b). The corresponding faulted loop size distributions measured from (a-b) are given in (e).

Table 3
Summary of faulted loop quantification analysis for the neutron-irradiated 21Cr32Ni model alloy.

Dose [dpa]	T [°C]	Faulted dislocation loop*			Cavity			$Cr_{23}C_6$ Precipitate		
		$\rho \pm 2\times\varepsilon$ [$\times 10^{22}\ m^{-3}$]	$D_{ave} \pm 2\times\varepsilon$ [nm]	D_{max} [nm]	$\rho \pm 2\times\varepsilon$ [$\times 10^{22}\ m^{-3}$]	$D_{ave} \pm 2\times\varepsilon$ [nm]	D_{max} [nm]	$\rho \pm 2\times\varepsilon$ [$\times 10^{22}\ m^{-3}$]	$D_{ave} \pm 2\times\varepsilon$ [nm]	D_{max} [nm]
17.1	376	0.30 ± 0.06	17.2 ± 1.8	57.6	0.39 ± 0.10	8.8 ± 1.1	19.9	0.25 ± 0.06	7.7 ± 0.5	13.9
35	378	0.97 ± 0.20	11.2 ± 1.2	36.1	0.42 ± 0.10	15.2 ± 0.8	31.7	0.42 ± 0.07	11.2 ± 0.6	21.1

*The faulted loop number density was reported after multiplying the number of loops counted in the RDF TEM images by 4 to take into account all possible loop orientations since only ¼ of the total faulted dislocation loops are visible, assuming a similar loop density in all possible loop orientations.

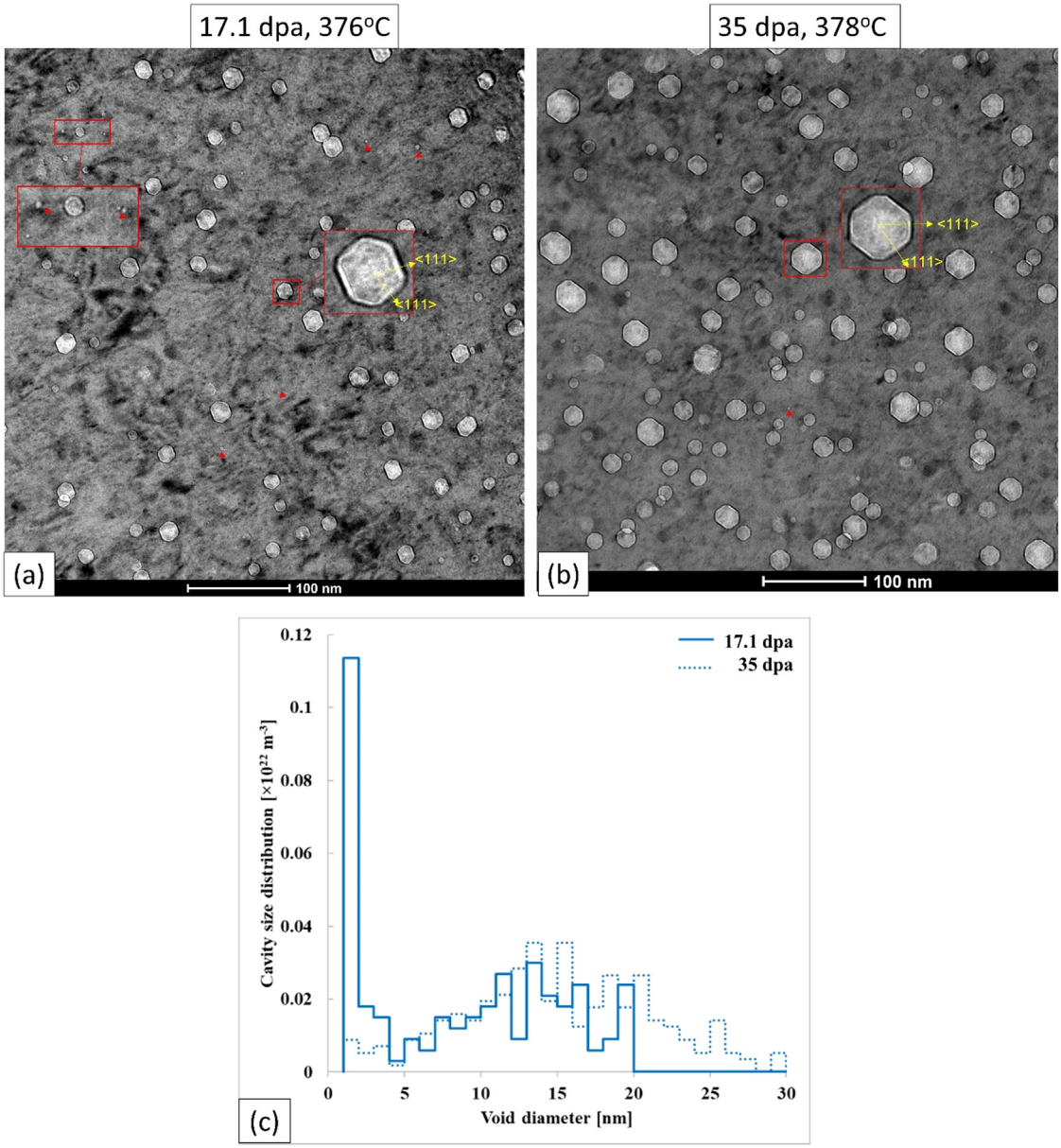

Fig. 6. Under-focus bright field TEM images showing cavity microstructure in 21Cr32Ni model alloy after fast neutron irradiation to (a) 17 dpa and (b) 35 dpa in the BOR reactor. Large cavities are observed to be faceted with facets lie along {111} planes, the close-packed plane in fcc as indicated with arrows. Some of the small spherical cavities are indicated with arrows. The corresponding cavity size distributions measured from (a-b) are given in (c).

that could reach the critical cavity size and grow via bias-driven growth [28]. The growth of small stable cavities to large cavities might be ascribed to an excess vacancy accumulation arising from fluctuations in the point defect flux or to an excess gas accumulation which eventually results in further vacancy absorption to maintain mechanical equilibrium in the cavity [28–30].

3.3. Microchemical changes in the BOR-60 irradiated 21Cr32Ni model alloy

The BOR-60 irradiation of 21Cr32Ni model alloy also resulted in the formation of Cr-rich precipitates as shown in STEM BF/DF and merged elemental maps of Fe, Cr and Ni presented in Fig. 7.

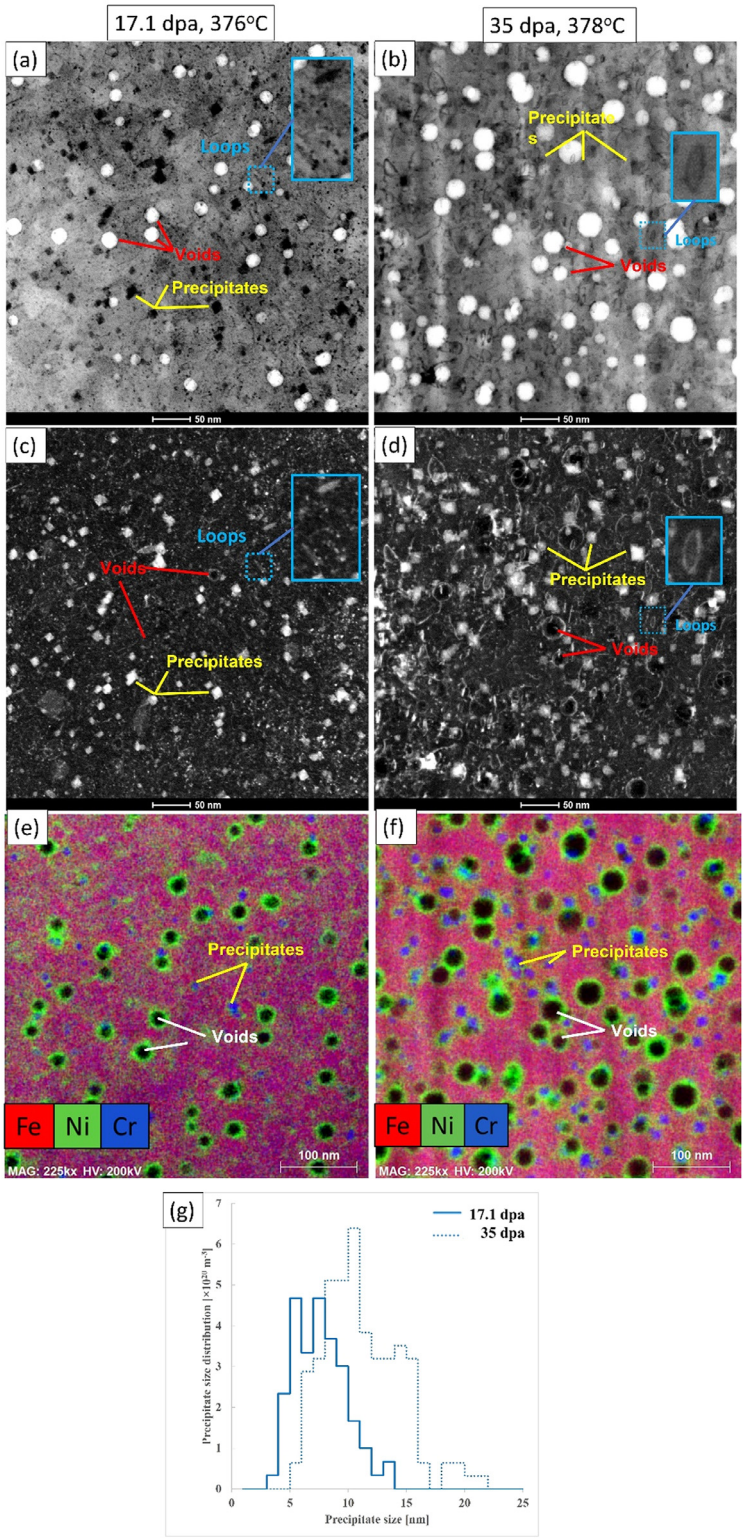

Fig. 7. (a-b) STEM Bright field TEM images and (c-d) STEM Dark-field TEM images recorded from the 21Cr32Ni model alloy microstructure after neutron-irradiation to 17 at ~376 °C and 35 dpa at ~378 °C in BOR-60 reactor showing neutron irradiation-induced dislocation loops, cavities and precipitates. Merged EDS maps of Fe, Ni and Cr given in (e-f) shows Ni segregation around the cavities, dislocations and precipitates (Scale bar=100 nm). Strong Cr signal from precipitates shows they are Cr-rich precipitates with the size distributions given in (g).

The Cr-rich precipitates at 35 dpa were observed to be larger than those at 17.1 dpa with a modest increase in number density, suggesting that existing precipitates grow with dose and few more precipitates nucleate. High-resolution TEM (HRTEM) images given in Fig. 8 show that these precipitates are also faceted with the facets are along {111} planes, similar to cavities. The faceting likely occurs to minimize the surface energy of these features. The additional diffraction spots visible in the HRTEM pattern suggest that the precipitates have an fcc crystal structure with a lattice parameter of ~10.7 nm, which is consistent with $Cr_{23}C_6$-type precipitates.

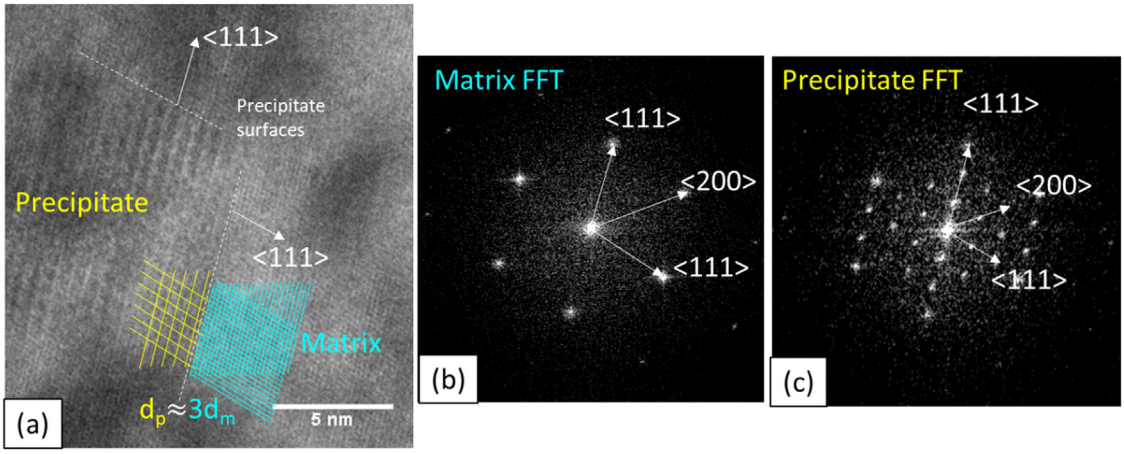

Fig. 8. (a) High-resolution TEM images showing the matrix and precipitate interface in 21Cr32Ni model alloy after neutron irradiation to 17.1 dpa at 376 °C. The image shows the {111} lattice of fcc-austenite matrix and precipitate. A schematic drawing is given for comparison to show the phase contrast interference from the {111} lattice planes and it shows that the d-spacing of the precipitate is ~3 times larger than that of the matrix. The precipitate surfaces are along the {111} planes. (b-c) show the fast-Fourier transform (FFT) images captured from the matrix and precipitate regions. The additional spots seen in (c) are indexed as fcc-type $Cr_{23}C_6$-type with a lattice parameter of ~10.7 nm.

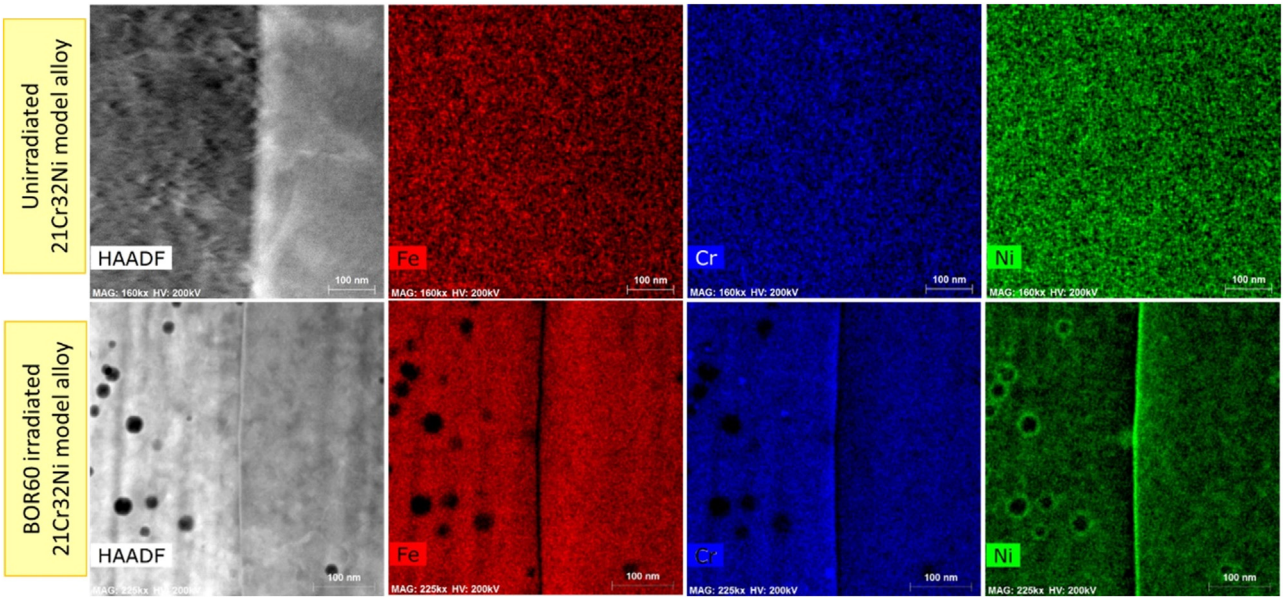

Fig. 9. EDS maps showing the elemental maps of Fe, Cr and Ni at the grain boundary in (Top) unirradiated 21Cr32Ni model alloy, and (bottom) after neutron irradiation in the BOR-60 reactor to 35 at 378 °C and shows Fe/Cr depletion and Ni segregation. Scale bar=100 nm.

Another microchemical change observed is the Ni enrichment at defects: dislocations, cavities, and precipitates. In fact, radiation-induced segregation of Ni was also observed at grain boundaries along with Fe and Cr depletion, as shown in Fig. 9. The enrichment of Ni and depletion of Cr in austenitic stainless steels after irradiation was reported by many authors [31–39]. G. Was and T. Allen described the kinetics of RIS in austenitic stainless steels by the – "inverse Kirkendall"- through which irradiation-induced vacancy-flux to grain boundaries causes diffusion of an equal flux of solute atoms in the opposite direction [33,34]. Because Ni is the slowest and Cr is the fastest diffuser in Fe-Cr-Ni system, Ni usually enriches, and Cr depletes at the defect sinks.

3.4. Comparison of neutron and dual-ion irradiation

The irradiation-induced microstructure (dislocations, cavities and microchemical changes) of the dual-ion irradiated 21Cr32Ni model alloy samples to 16.6 dpa was characterized using TEM and compared with the microstructure observed after the BOR-60 neutron-irradiated 21Cr32Ni model alloy to 17.1 dpa. The summary of this examination is presented in Fig. 10 -Fig. 14.

3.4.1. Comparison of dislocation and cavities

Fig. 10, Fig. 11 and Fig. 12 show the evolution of dislocations and cavities in 21Cr32Ni model alloy after dual-ion irradiation to 16.6 dpa compared with that seen under the BOR-60 neutron irradiation to the similar dose.

It is clear that dual-ion and neutron irradiation of 21Cr32Ni model alloy produce qualitatively similar dislocation morphologies, i.e. both dislocation microstructures consist of high-density network dislocation and dislocation loops that are mainly {111}-type faulted in nature, as highlighted with red arrows in Fig. 10. For better visibility of the dislocation loops and comparison, a series of RDF TEM images were captured from each dual-ion irradiation

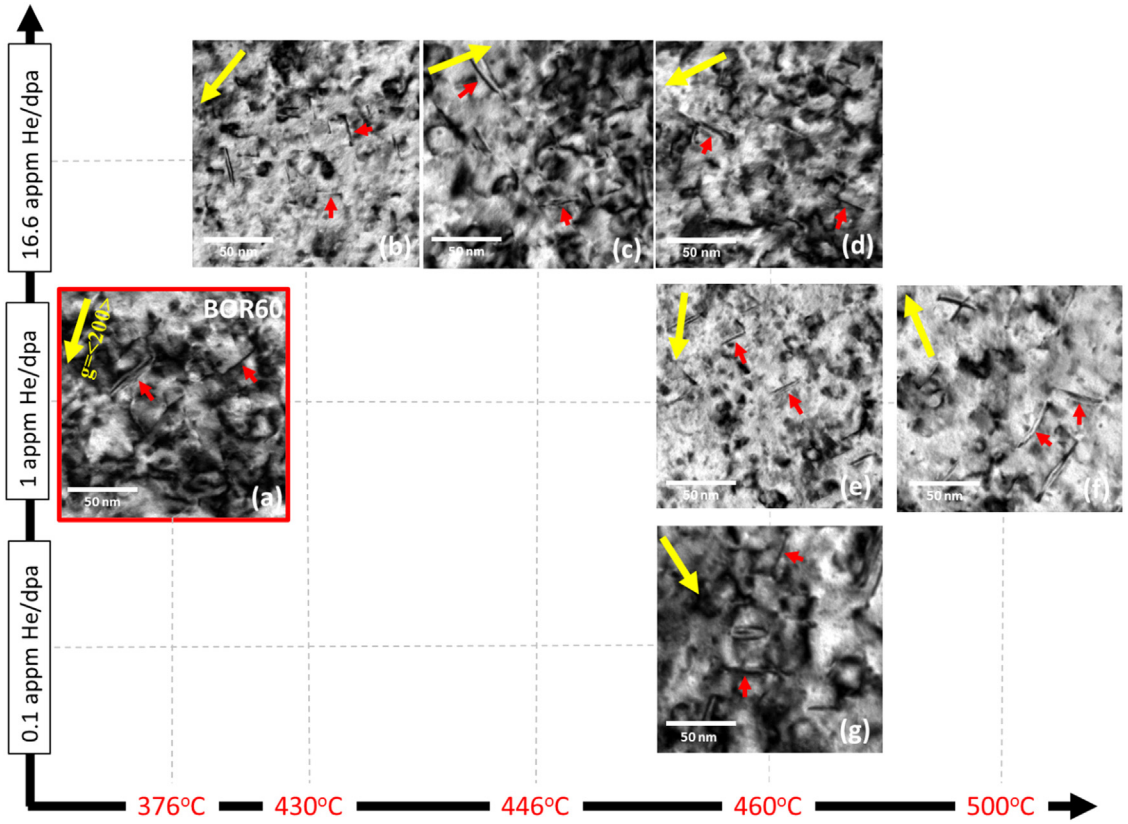

Fig. 10. Bright-field TEM image table showing radiation-induced dislocation morphology in dual-ion irradiated 21Cr32Ni model alloy to 16.6 dpa as a function of irradiation temperature and helium injection rate (Scale bar=50 nm). The dislocation morphology produced by the fast neutron irradiation to 17.1 dpa is highlighted for comparison. The images recorded using g=<200> diffraction vectors near the [110] zone axis (indicated with yellow arrows). Some of the {111}-type edge-on dislocation loops are highlighted with red arrows.

condition and presented in Fig. 11. Because the rel-rods originate from the stacking faults, they make visible only the faulted loops. Fig. 11 reveals numerous small dislocation loops in the dual-ion irradiated 21Cr32Ni model alloy samples especially at 16.6 appm He/dpa ratio, suggesting that faulted loop nucleation is promoted with increasing helium injection rate. For the conditions of 0.1 and 1 appm He/dpa, the faulted loops were relatively larger and less numerous, consistent with what was observed in the BOR-60 neutron-irradiated sample.

To further extend our understanding of the He/dpa ratio influence on faulted dislocation loop formation and growth, cavity morphologies were also compared, as shown in Fig. 12. The cavity microstructures in the dual-ion irradiated 21Cr32Ni model alloy samples showed noticeable differences compared to what was seen in the neutron-irradiated sample, depending on the helium injection rate. Note that large and faceted cavities previously found in the BOR-60 irradiated samples were only observed in the dual-ion irradiated 21Cr32Ni model alloy sample for the condition of 0.1 appm He/dpa, which is an order of magnitude smaller than the estimated helium generation rate in the BOR-60 reactor. Upon increasing He/dpa ratio to 1 and 16.6 appm He/dpa, the cavity microstructure was remarkably different than that seen in the BOR-60 neutron-irradiated sample to the similar dose where small-spherical cavities are over-nucleated in the microstructure, resulting in a much higher cavity density and smaller size.

For quantitative comparison, the faulted loop and cavity size distributions are plotted in Fig. 13. The number density and size of the faulted dislocation loops and cavities in the dual-ion irradiated 21Cr32Ni model alloy samples showed the best match with the BOR-60 neutron irradiation for the condition of 0.1 appm He/dpa consistent with the TEM observations. In contrast, for the conditions of 1 and 16.6 appm He/dpa, dual-ion irradiation resulted in a higher number density of faulted dislocation loops and cavities compared to the fast neutron irradiation, regardless of the irradiation temperature. The increase in cavity population at high helium injection rates can be attributed to the increase in cavity nucleation rate, likely due to the increase in the amount of helium trapping at irradiation-induced vacancies. In other words, as the helium content increases, the probability of cavity nucleation also increases, causing the formation of many small cavities in the microstructure [40,41]. Also, as more helium atoms are trapped at vacancies, it may lead to a relatively lower interstitial-vacancy recombination rate which means that a higher fraction of interstitials can remain in the matrix to promote faulted loop formation.

Fig. 13 also shows that an increase in irradiation temperature slightly decreases the number densities of faulted dislocation loops and cavities and brings their size distributions closer to the size distribution seen in neutron-irradiated sample, although the change is small. The decrease in cavity number density at elevated temperatures can be attributed to the reduction of vacancy supersaturation (i.e. the fraction of excess vacancies produced as a result of irradiation relative to the thermal vacancies in the material) since defects are annihilated more rapidly at sinks. Therefore, fewer vacancies will be available in the matrix to make cavities to grow at higher temperatures. For the case of dual-ion irradiation where helium also promotes cavity nucleation rate, the decrease in vacancy concentration reduces He-V clustering as previously shown in the literature using reaction rate theory models [42,43].

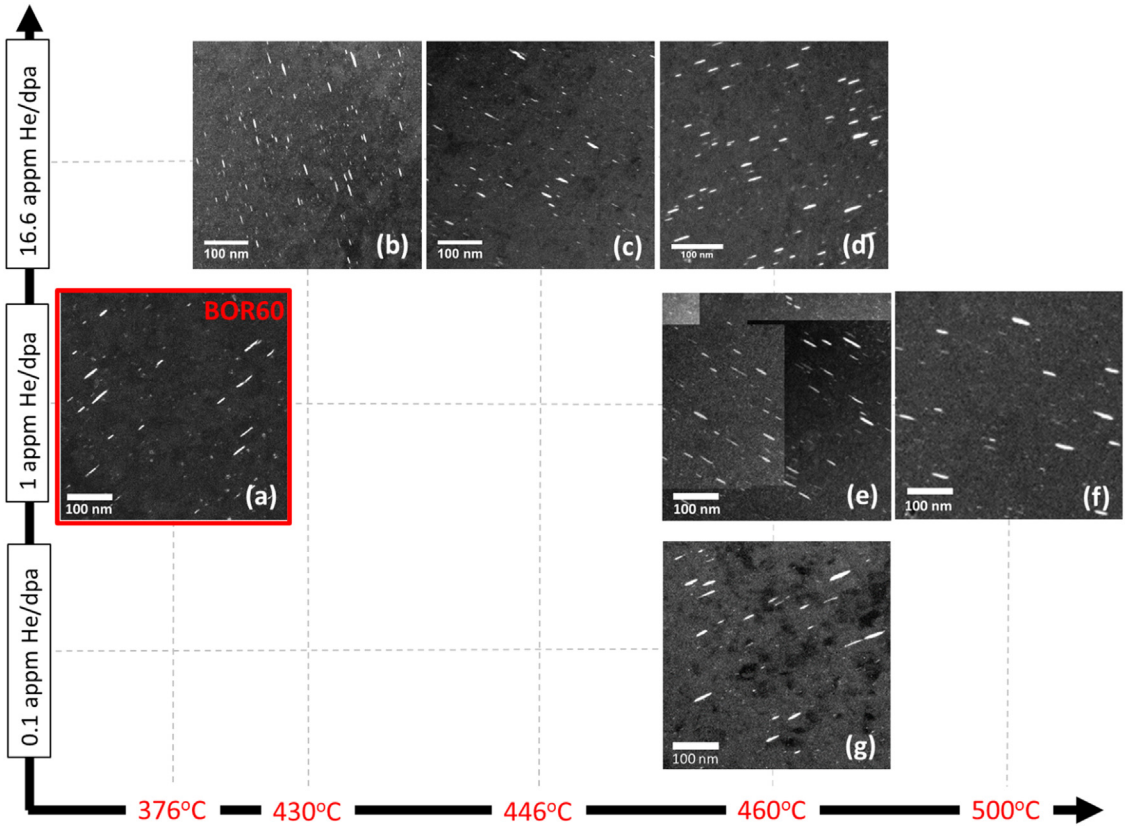

Fig. 11. Rel-rod dark-field TEM images showing faulted dislocation loops in the dual-ion irradiated 21Cr32Ni model alloy to 16.6 dpa as a function of irradiation temperature and helium injection rate (scale bar=100 nm). The faulted loops formed by the BOR-60 neutron irradiation to 17.1 dpa is highlighted for comparison. The corresponding foil thicknesses are calculated as (a)132 nm, (b)74 nm, (c)104 nm, (d)98 nm, (e)140 nm, (f)62 nm and (g)100 nm.

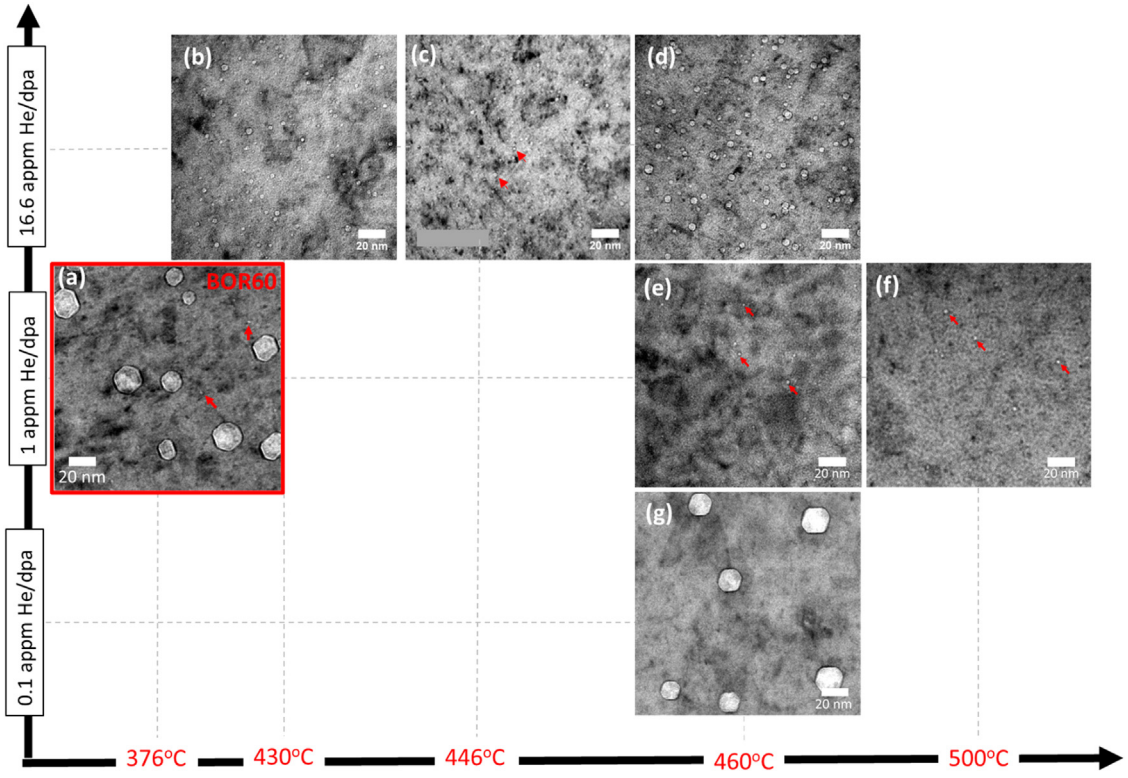

Fig. 12. Bright-field under-focused TEM images showing irradiation-induced cavities in the dual-beam irradiated 21Cr32Ni model alloy to 16.6 dpa as a function of irradiation temperature and helium injection rate (Scale bar=20 nm) in comparison with the cavities formed after the BOR-60 irradiation to 17.1 dpa at 376 °C. Some of the small cavities (~1–2 nm) are highlighted with the arrows. The corresponding foil thicknesses are calculated as (a)132 nm, (b)74 nm, (c)104 nm, (d)98 nm, (e)140 nm, (f)62 nm and (g)100 nm.

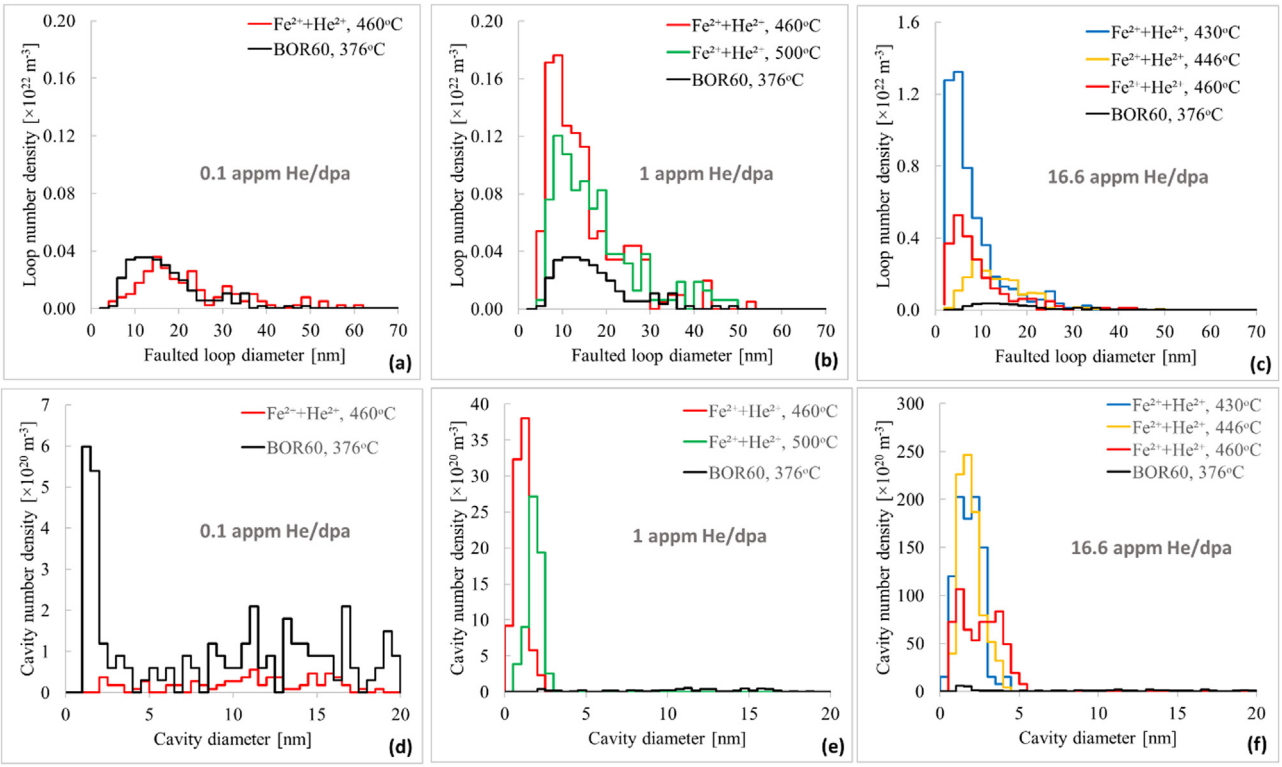

Fig. 13. (a-c) Faulted loop size distributions and (d-f) cavity size distributions in dual-ion irradiated 21Cr32Ni model alloy with 0.1, 1 and ~16.6 appm He/dpa in comparison with the BOR-60 irradiated 21Cr32Ni of the same heat,.

The experimental observations indicate that the emulation of fast neutron irradiation of austenitic stainless steels requires a reduction in helium injection rate in addition to the application of temperature shift. This is in contrast to what was observed in bcc type ferritic/martensitic steels where higher He/dpa ratio was needed to achieve a similar microstructure [11]. When considering the significant damage rate difference between dual-ion and neutron irradiation ($(5–10)\times10^{-4}$ dpa/s vs. $\sim1\times10^{-6}$ dpa/s), keeping the He/dpa ratio constant in the former causes the corresponding helium injection rate to be a factor of ~500–1000 higher than the latter. Because the defect production rate is also high in dual-ion irradiation, it is likely that helium atoms are quickly trapped by irradiation-induced vacancies, thus enhancing the cavity nucleation rate, and suppressing cavity growth. The increase in He-V clustering would result in a higher fraction of interstitials available in the matrix to promote the formation of faulted dislocation loops, causing a reduction in their average diameters. Therefore, the emulation of neutron irradiation of fcc and bcc type alloys using dual-ion irradiation should be handled distinctly. The exact reason for the difference between the two crystal structures is not known, but it is possibly related to differences between helium and vacancy migration in the two crystal structures which requires further investigation.

3.4.2. Comparison of microchemical evolution

In this section, the microchemical evolution observed in both types of microstructures is qualitatively compared and presented. However, it is important to remind the reader that the temperature shift used in this study is 50 °C-80 °C and it is much smaller than the suggested temperature shift for RIS which is ~270 °C [1,2]. Therefore, the data provided in this section is meant only to give some insights for the reader into the capability of dual-ion irradiation to qualitatively compare the microchemical evolution as reference.

The elemental maps shown in Fig. 14 show the qualitative comparison of microchemical changes observed in the 21Cr32Ni model alloy microstructure after dual-ion and neutron irradiation. Fig. 14 shows that the Ni enrichment at cavities in the BOR-60 irradiated samples also appears in the dual-ion irradiated 21Cr32Ni model alloy sample for the irradiation condition of 0.1 appm He/dpa:460 °C. In contrast, no distinguishable Ni signal was observed around the cavities in other dual-ion irradiated samples, likely because the Ni signal around small cavities was masked by the strong Ni signal from the austenitic matrix.

No evidence of Cr-rich carbide precipitates was found in any dual-ion irradiated 21Cr32Ni samples examined in this study, suggesting that the stability of these precipitates decreases when the alloy is subjected to irradiation at very high damage rates relative to what occurs under neutron irradiation. Irradiation-induced precipitate growth is thought to be governed by the competition of the two major processes [44,45]: (1) irradiation-enhanced solute diffusion due to the increase in point defect concentrations and (2) irradiation-induced ballistic dissolution. Note that irradiation-induced dissolution increases linearly with damage rate, whereas precipitate growth does not have such a straightforward relationship to damage rate. For the case of dual-ion irradiation, it is possible that precipitate dissolution is the dominant process relative to radiation-enhanced diffusion at high damage rates. Because solute diffusion also increases with increasing irradiation temperature, this also suggests that the required temperature shift to emulate neutron-induced precipitation may be higher than that used to emulate neutron-induced dislocations and cavities in this study.

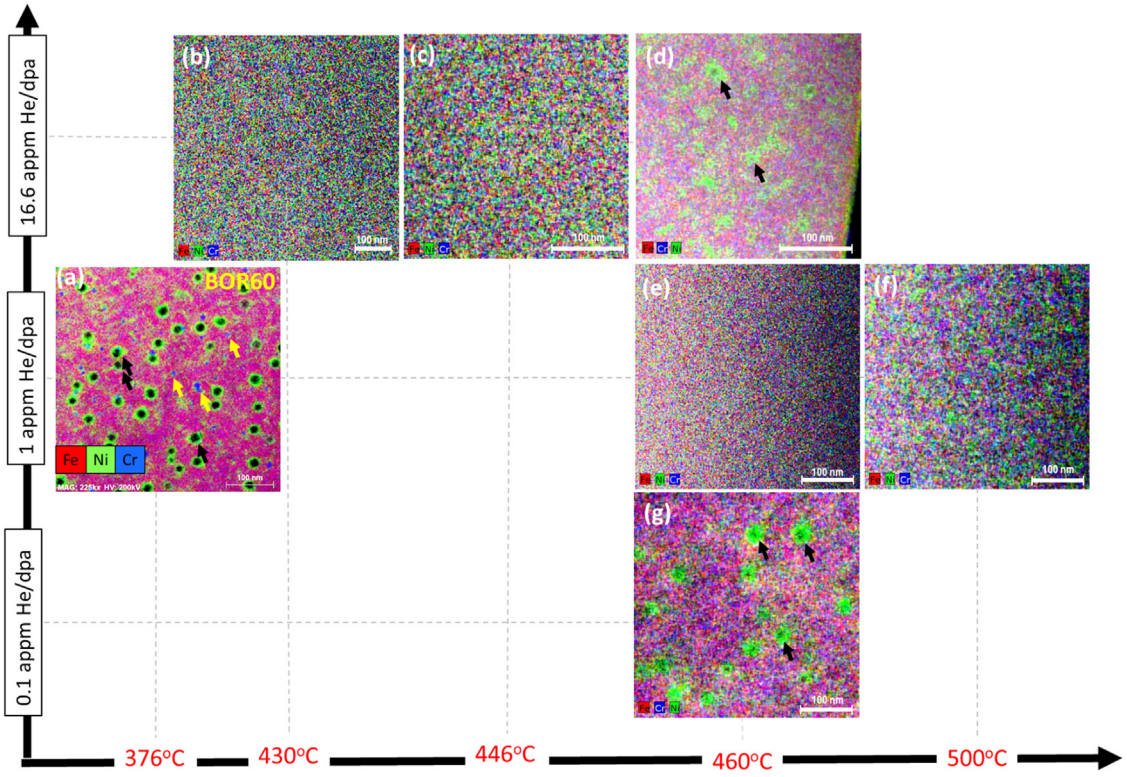

Fig. 14. S/TEM EDS merged elemental maps of Fe, Cr and Ni showing Ni distribution around the cavities (green color and highlighted with black arrows) and Cr-rich precipitates (blue color, highlighted with yellow arrow) in 21Cr32Ni sample after the BOR-60 neutron irradiation to 17.1 dpa and the dual-ion irradiation to 16.6 dpa at various temperatures and He/dpa ratios. The scale bar=100.

4. Summary and conclusion

In this paper, the irradiation-induced microstructure in fast-neutron irradiated austenitic 21Cr32Ni model alloy was examined up to 35 dpa using TEM. The 17.1 dpa neutron-induced microstructure was then compared with the microstructures seen in a series of 16.6 dpa dual-ion irradiated 21Cr32Ni model alloy microstructures with different He/dpa and various temperature shifts since the dual-ion irradiation experiments were conducted with $\times$ 500–1000 higher damage rates than that of reactor irradiation. The temperature shift used in dual-ion irradiation was selected to emulate neutron-induced dislocation loop and cavity microstructures. The key findings are summarized below:

- Both fast neutron and dual-ion irradiation of austenitic 21Cr32Ni model alloy resulted in the formation of dislocations (dislocation network and faulted dislocation loops), cavities, Ni enrichment and Fe/Cr depletion at point defect sinks. Cr-rich carbide precipitates observed in neutron-irradiated samples at low damage rates did not form during ion irradiation at high damage rates regardless of He/dpa ratio used.
- For the same He/dpa ratio, increasing the irradiation temperature decreased the number density of faulted dislocation loops and cavities. The average diameter of the cavities and dislocation loops did not change significantly with increasing irradiation temperature.
- For the same irradiation temperature, increasing the He/dpa ratio resulted in over-nucleation of small spherical cavities and an increase in the number density of small faulted dislocation loops.
- When irradiation dose and He/dpa ratio in dual-ion and the BOR-60 neutron irradiation kept similar, the dual-ion irradiation at 460 °C resulted in an over-nucleation of small spherical cavities and a higher density of small, faulted dislocation loops in the 21Cr32Ni model alloy microstructure relative to the BOR-60 fast neutron irradiation at ~376 °C, showing that the application of temperature shift by itself is unable to reproduce neutron-induced faulted dislocation loops and cavities as was predicted by the invariance equations. When the He/dpa ratio was reduced at high damage rates, a close match was found in both faulted dislocation loop and cavity microstructures, indicating that the helium injection rate must also be optimized in addition to the temperature shift to be able to emulate the neutron-induced austenitic model alloy microstructure.
- Neutron-induced Cr-rich precipitates were not observed in any dual-ion irradiated microstructures examined in this study, suggesting that a higher temperature shift is essential to emulate neutron-induced microchemical evolution.

Declaration of Competing interest

The authors declare that they have no known competing financial interests or personal relationships that could have appeared to influence the work reported in this paper.

CRediT authorship contribution statement

Muhammet Ayanoglu: Formal analysis, Investigation, Writing – original draft, Writing – review & editing. **Arthur T. Motta:** Supervision, Writing – review & editing.

Data Availability

No data was used for the research described in the article.

Acknowledgements

This work was supported by a DOE NEUP Integrated Research Project (IRP) by the U.S. Department of Energy under award number DE-NE0000639. We thankG. S. Was, Stephen Taller and the Michigan Ion Beam Laboratory stafffor carrying out the bulk-ion irradiation experiments, for their helpful discussions and for providing the bulk ion irradiated samples with helium implantation profiles, Emanuelle Marquis for providing APT measurements, Trevor Clark and Jenn Gray at MCL-PSU for their help on sample preparation, Kevin Field, Jesse Warden and Kory Linton for their help on the FIB sample preparation and TEM examination of the BOR-60 irradiated samples.

References

[1] L.K. Mansur, Nucl. Tech. 40 (1978) 5–33.
[2] L.K. Mansur, J. Nucl. Mater. 216 (1994) 97–123.
[3] N.H. Packan, K. Farrell, J.O. Stiegler, J. Nucl. Mater. 78 (1978) 143–155.
[4] G.S. Was, et al., J. Nucl. Mater. 300 (2002) 198–216.
[5] S. Taller, et al., J. Nucl. Mater. 527 (2019) 151831.
[6] S. Taller, G. Was, J. Nucl. Mater. 198 (2020) 47–60.
[7] J. Cao, W. Geng, J. Nucl. Mater. 478 (2016) 13–25.
[8] L. Ventelon, B. Wirth, C. Domain, J. Nucl. Mater. 351 (2006) 119–132.
[9] X.T. Zu, et al., Phys. Rev B 80 (2009) 054104.
[10] ASTM B409-06, Standard Specification for Nickel-Iron-Chromium Alloy Plate, Sheet, and Strip, 2016, ASTM International, West Conshohocken, PA, 2016 www.astm.org.
[11] S. Taller, et al., Nucl. Instrum. Methods Phys. Res. Sect. B Beam Interact. With Mater. Atoms. 412 (2017) 1–10.
[12] J. Dryzek, C. Wesseling, E. Dryzek, B. Cleff, Mater. Lett. 21 (2) (1994) 209–214.
[13] M.P. Surh, J.B. Sturgeon, W.G. Wolfer, J. Nucl. Mater. 328 (2004) 107–114.
[14] J.F. Ziegler, J.P. Biersack, SRIM2008 Program, IBM Corp, Yorktown, NY, 2008.
[15] R.E. Stoller, et al., Nucl. Instrum. Methods B 310 (2013) 75–80.
[16] H.R. Brager, F.A. Garner, M.L. Hamilton, J. Nucl. Mat. 133-134 (1985) 594–598.
[17] M.H. Mayoral, M.L.Jenkins Z.Yao, M. Kirk, Phil. Mag. 88 (21) (2008) 2881–2897, doi:10.1080/14786430802380477.
[18] M. Jin, P. Cao, M.P. Short, Scripta Mat 163 (2019) 66–70.
[19] H. Takahashi, N. Hashimoto, Mater. Trans. 34 (1993) 1027–1030 JIM, doi:10.2320/matertrans1989.34.1027.
[20] C.A. Schneider, W.S. Rasband, K.W. Eliceiri, NIH Image to ImageJ: 25 years of image analysis, Nat. Methods 9 (2012) 671–675.
[21] M. Ayanoglu, A.T. Motta, J. Nucl. Mater. 510 (2018) 297–311.
[22] C.J. Ulmer, A.T. Motta, J. Nucl. Mater. 498 (2018) 458–467.
[23] S. Hayakawa, et al., Nucl. Mater. Energy 9 (2016) 581–586.
[24] T. Nogaret, C. Robertson, D. Rodney, Philos. Mag. 87 (2007) 945–966.
[25] A. Kubota, W.G. Wolfer, Mater. Sci. Eng. A 400-401 (2005) 362–365.
[26] J.L. Strudel, J. Washburn, Phil. Mag 9 (99) (1964) 491–506, doi:10.1080/14786436408222960.
[27] A.J. Foreman, J.V. Sharp, Phil. Mag 19 (931) (1969).
[28] A. Hishinuma, L.K. Mansur, J. Nucl. Mater. 118 (1983) 91–99.
[29] L.K. Mansur, W.A. Coghlan, J. Nucl. Mater. 119 (1983) 1–25.
[30] R. Stoller and G. Odette, "A comparison of the relative importance of helium and vacancy accumulation in void nucleation," in *Radiation-Induced Changes in Microstructure: 13th International Symposium (Part I)*, ed. F. Garner, N. Packan, and A. Kumar (West Conshohocken, PA: ASTM International, 1987), 358–370.
[31] R.A. Johnson, N.Q. Lam, Phys. Rev. B 13 (10) (1976) 4364–4375.
[32] N.Q. Lam, P.R. Okamoto, H. Wiedersich, et al., Metall. Mater. Trans. A 9 (1978) 1707–1714, doi:10.1007/BF02663400.
[33] G. Was, T.R. Allen, J.T. Busby, J. Gan, D. Damcott, D. Carter, M. Atzmon, E.A. Kenik, J. Nucl. Mater. 270 (1999) 96–114.
[34] T. Allen, J.T. Busby, G.S. Was, E.A. Kenik, J. Nucl. Mater. 255 (1998) 44–58.
[35] W. Busby, Kenik, J. Nucl. Mater. 302 (2002) 20–40.
[36] K. Fujii, K. Fukuya, J. Nucl. Mater. 469 (2016) 82–88.
[37] D.J. Edwards, et al., J. Nucl. Mater. 317 (2003) 32–45.
[38] F. Fukuya, Nishioka, Kitsunai, J. Nucl. Sci. Technol. 43 (2006) 159–173.
[39] Z. Jiao, G.S. Was, Acta Mater. 59 (2011) 1220–1238.
[40] D. Stewart, R. Stoller, J. Nucl. Mater 417 (2011) 1110–1114.
[41] L.K. Mansur, E.H. Lee, P.J. Maziasz, A.P. Rowcliffe, J. Nucl. Mater. 141-143 (1986) 633–646.
[42] W.A. Coghlan, L.K. Mansur, J. Nucl. Mater. 122 (1984) 495–501.
[43] N. Ghoniem, S. Sharafat, J.M. Williams, L.K. Mansur, J. Nucl. Mater. 117 (1983) 96–105.
[44] R.S. Nelson, J.A. Hudson, D.J. Mazey, J. Nucl. Mater 44 (1972) 318–330.
[45] K.C. Russell, J. Nucl. Mater. 83 (1979) 176–185.